# Buckling and free vibration study of variable and constant-stiffness cylindrical shells

Labans, Edgars; Bisagni, Chiara

**Important note**
To cite this publication, please use the final published version (if applicable).
Please check the document version above.

# Accepted Manuscript

Buckling and free vibration study of variable and constant-stiffness cylindrical shells

Edgars Labans, Chiara Bisagni

Please cite this article as: Labans, E., Bisagni, C., Buckling and free vibration study of variable and constant-stiffness cylindrical shells, *Composite Structures* (2018), doi: https://doi.org/10.1016/j.compstruct.2018.11.061

# BUCKLING AND FREE VIBRATION STUDY OF VARIABLE AND CONSTANT-STIFFNESS CYLINDRICAL SHELLS

**Edgars Labans[1] and Chiara Bisagni[2]**

Delft University of Technology, Faculty of Aerospace Engineering, 2629 HS, Delft, The Netherlands

[1]e.labans@tudelft.nl, [2]c.bisagni@tudelft.nl

## Abstract

The ability to steer carbon fibre tapes, varying the tow angle, can widen the designs possibilities of cylindrical shells that are one of the main components of aerospace structures. This research presents experimental and numerical investigation of two carbon fibre reinforced plastic cylindrical shells – a cylinder with conventional layup made of unidirectional prepreg and a variable-stiffness cylinder manufactured by applying fibre placement technology. The shells were tested in compression until buckling and later subjected to a vibration analysis. Load-shortening curves and buckling shapes were acquired during the compression tests, while the natural frequencies and the mode shapes were measured during the vibration tests. Both tests provide a useful data set of the mechanical response of the cylinders which can be applied for further validation of models. The acquired experimental results were compared to a simple, approximated numerical model of the variable-stiffness cylinder showing good correlation with the test results.

---

[1] Corresponding author.

1

## 1. Introduction

Since their development in late 1980s Automated Fiber Placement (AFP) machines are widely used to manufacture large aerospace structures like wing sections, fuselages and cylindrical shells for rocket launch vehicles [1-2]. The process consists of placing bands of unidirectional fibre prepreg on the surface of a mould or tooling.

Only recently the fiber-steering capabilities were applied to intentionally produce spatially varying fiber orientations within a single ply and generate variable-stiffness laminates for improved structural performance. Initial benefits of curvilinear fibers were reported by Hyer and Lee [3], Hyer and Charette [4], and later by Schueler and Hale [5] performing numerical studies. Tatting and Gürdal [6] conducted experimental work on design, manufacturing and testing of flat variable-stiffness plates. They demonstrated that substantial structural improvements in strength, stiffness and buckling load could be reached by applying curved fibers. Other researchers have also contributed to the knowledge of flat tow-steered laminate plates [7-11]. Recent progress in variable-stiffness design and optimization of fiber-reinforced composite structures was summarized by Ghiasi et. al. [12] and Sabido et. al. [13] considering stiffness, strength, buckling, dynamic, thermal and combined design criteria. A review by Lozano et al. [14] covers mostly design and manufacturing issues.

Although the number of studies focus on flat and small scale variable-stiffness specimens, only few studies cover cylindrical shells. On the contrary, constant stiffness composite shells were investigated for decades resulting in numerous experimental and numerical studies [15-19].

Several articles on design, manufacturing and testing of two variable-stiffness Carbon Fibre Reinforced Plastic (CFRP) cylinders in compression were published by Wu [20,21].

2

One of the cylinders was manufactured allowing overlaps, while a second one was made without overlaps to maintain constant thickness. Subsequent research by White was performed with the same cylinders to assess the influence of large cut-outs and deep post-buckling behaviour [22].

Variable-stiffness cylinders under the bending load were investigated in the works of Blom [23]. Circumferential stiffness variation was introduced to increase buckling load in bending up to 17% compared to the best optimized constant stiffness cylinder. Another study on the bending of the variable-stiffness cylinders demonstrate that manufacturing imperfections can significantly decrease the gain of fibre steering [24].

Most of the works on variables stiffness composite shells are based on numerical modelling. For example, Rouhi [25] evaluated the effect of radius and length/radius ratio for cylinders in pure bending. Main results of the optimisation indicate that variable-stiffness cylinders made by fibre steering outperform optimized constant stiffness examples, providing up to 38% higher buckling load. Relevant research by Khani [26] describes a method of circumferential tailoring of cylinders subjected to bending, compression or torsion. The method also considers strength constraints and manufacturing restrictions. The authors compared buckling loads of the variable-stiffness cylinders to the constant stiffness alternative. It was demonstrated that the largest improvement of the buckling load up to 30% can be achieved for the shells subjected to bending load case. Buckling load in axial compression usually benefits less from variable-stiffness design, achieving up to 18% gain. Similar study of Sedat and Altan [27] shows possible advantages on mechanical performance of variable-stiffness cylinders under several load cases like bending, torsion and compression. Also the article of Sun and Hyer [28] shows that implementation of varying fibre orientation in elliptical cylinders has the potential to increase axial buckling load. In the

3

work of White and Weaver [29], optimized variable-angle tows are used in the laminate of cylindrical shells to reduce the sensitivity of these structures to geometrical imperfections.

Taking into account that test data on variable-stiffness shells are rare, the aim of the current study is to obtain experimental results on the buckling and free-vibration behaviour of variable-stiffness and constant stiffness cylinders. Additionally, simplified finite element models were developed to predict the stiffness and buckling load of the tested shells.

The brief outline of the article is as follows: 2nd chapter describes the properties of the analysed cylinders; 3rd chapter provides the measurements of the initial geometrical imperfections; 4th chapter reports the numerical models; 5th chapter describes the experimental test set-up and 6th chapter contains the results and discussions. Conclusions are then reported at the end.

## 2. Cylindrical shells

The investigated cylinders were manufactured by the Dutch National Aerospace Laboratory (NLR). The specimens have an inner diameter of 600 mm and a length of 790 mm. A photo of the cylinders is reported in Figure 1.
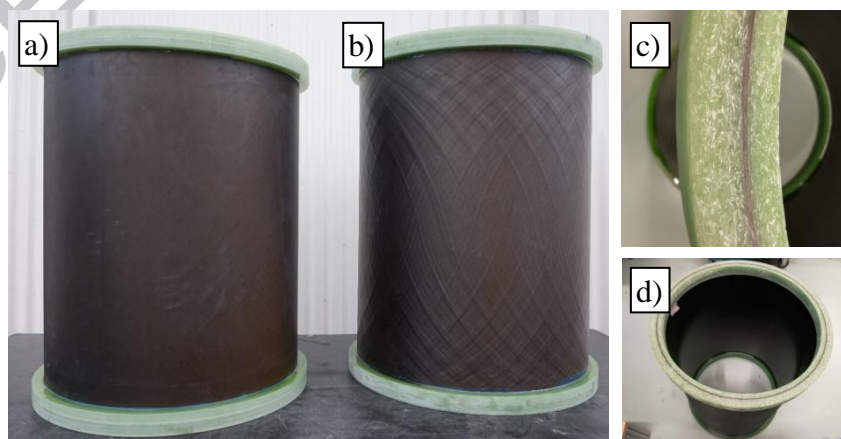


Figure 1. Cylindrical shells: a) the constant-stiffness cylinder;
b) the variable-stiffness cylinder; c) potting – close view; d) cylinder – top view

Both cylinders are composed of 8 layers of AS4/8552 CFRP prepreg with the average thickness of 0.181 mm. The mechanical properties of AS4/8552 CFRP prepreg are summarized in Table 1 [32]. After applying the lay-up on the steel mandrel with an automated robot arm, cylinders were placed in an autoclave for final curing.

Table 1. Material properties of AS4/8552 prepreg

| $E_{11}$ (GPa) | $E_{22}$ (GPa) | $G_{12}$ (GPa) | $\nu_{12}$ (−) | $\rho$ (kg/m$^3$) |
|---|---|---|---|---|
| 141 | 10.3 | 4.5 | 0.3 | 1580 |

The constant-stiffness cylinder has a traditional lay-up of $[\pm45/\ 0/\ 90]_s$ which means that the fibres are placed straight (without variation of the tow angle within a single layer) and there is no thickness variation in the cylinder. On the contrary the variable-stiffness cylinder has the lay-up of $[\pm45/\ \pm\varphi(x)]s$, where $\pm\varphi(x)$ is a steered ply with constant course width. Stiffness of the shell varies along the axial direction. The fibre angle at the top and the bottom of the cylinder is $60^0$ and in the middle it is $15^0$. The unwrapped plot of the two steered layers is shown in Figure 2. The course has a width of 63.5 mm and a constant curvature variation in two sections along the axial direction. Due to technical limitations of the available fibre lay-up machine, the course width of 63.5 mm consists of 5 smaller courses with the width of 12.5 mm lied parallel to each other. The following course of 63.5 mm is then shifted along the circumferential direction, creating the overlap at the ends of cylinder. Due to the overlaps, the laminate thickness nearly doubles at both ends of the cylinder.

Axial direction
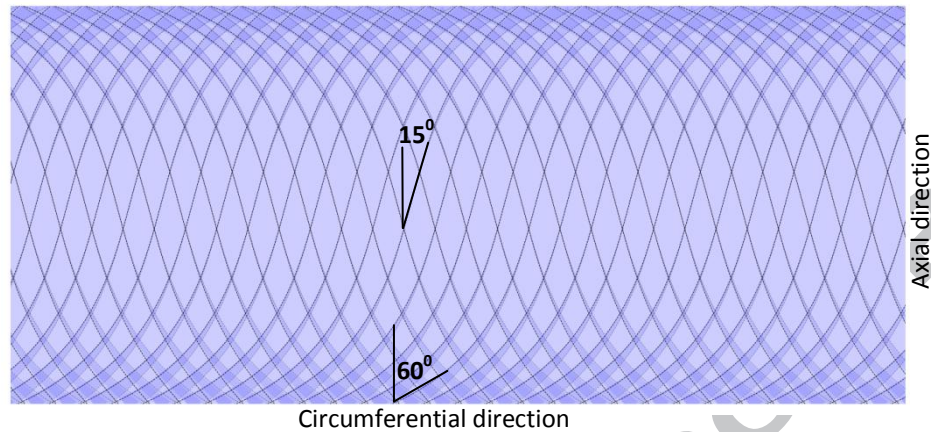
15⁰

60⁰

Circumferential direction

Figure 2. The path of the steered fibres

Both cylinders have an end-potting made of epoxy resin to be able to apply the load on the structure. Outer thickness of the potting is equal to 25 mm and inner thickness is equal to 15 mm. The potting covers 40 mm of the cylinder height at each end.

It should be noted that the variable-stiffness cylinder was not optimized for maximal stiffness or buckling load. The main purpose of this cylinder was the feasibility study of the manufacturing method combining parallel and shifted tows.

## 3. Geometrical imperfections

The initial geometrical imperfections were measured before the compression tests from outer and inner side of the cylinders. The imperfections from the outer side were measured by Digital Image Correlation (DIC) system, and from inner side by laser distance sensor.

The test set-up for the surface imperfection scan using VIC3D [30] DIC system is shown in Figure 3. Fine speckle pattern was applied on the surface of the cylinders to provide tracking points for the DIC system. The average speckle dot size was 3 mm with filling density of 20%. The surface was measured sequentially capturing approximately $130^0$ of the cylinder area in one shot and turning the cylinder by $90^0$ four times. Final array of the

data points was combined in VIC 3D software to obtain the whole 3D shape of the cylinder.
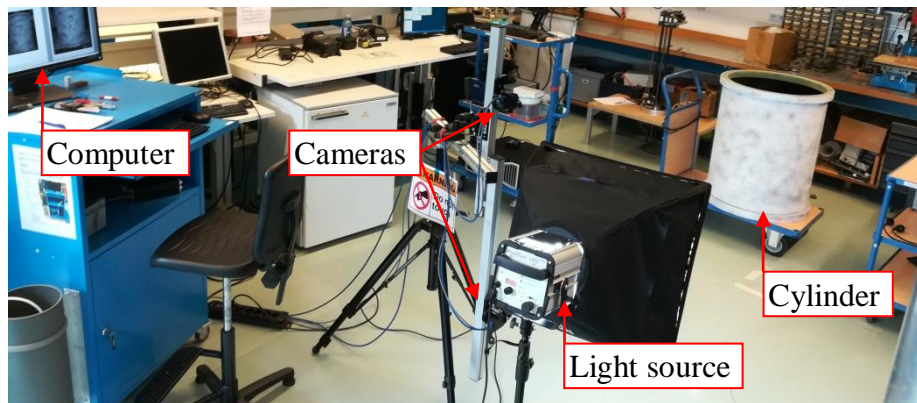


Figure 3. Test set-up for measuring external geometric imperfections using DIC

Post-processing of the imperfection data was performed in Matlab. The best-fit radius of the cylinder was found, and the measured geometric imperfections were characterized as deviation from the radius of the perfect cylinder. The unwrapped surfaces of the cylinders with imperfection colour plots are given in Figure 4. Positive values on the colour bar indicate that imperfections are larger than the perfect radius and negative values that they are smaller. It is worth noting that the constant-stiffness cylinder in Figure 4.a is ovalized along the whole vertical axis and imperfection values reach ±1 mm, which is approximately 66 % of the cylinder wall thickness.

Imperfection plot of the variable-stiffness cylinder in Figure 4.b has sufficient resolution to distinguish tows of overlapped fibres. It can be seen that the global out-of-plane imperfections exceed the local imperfections caused by fibre overlaps. The cylinder is ovalized in the lower part with maximal outer imperfection values of 1.5 mm and bent inwards in two wide areas in the middle of longitudinal coordinate with imperfection values reaching -1 mm. These maximum imperfection values are close to the thickness of the cylinder wall in the area without overlaps.
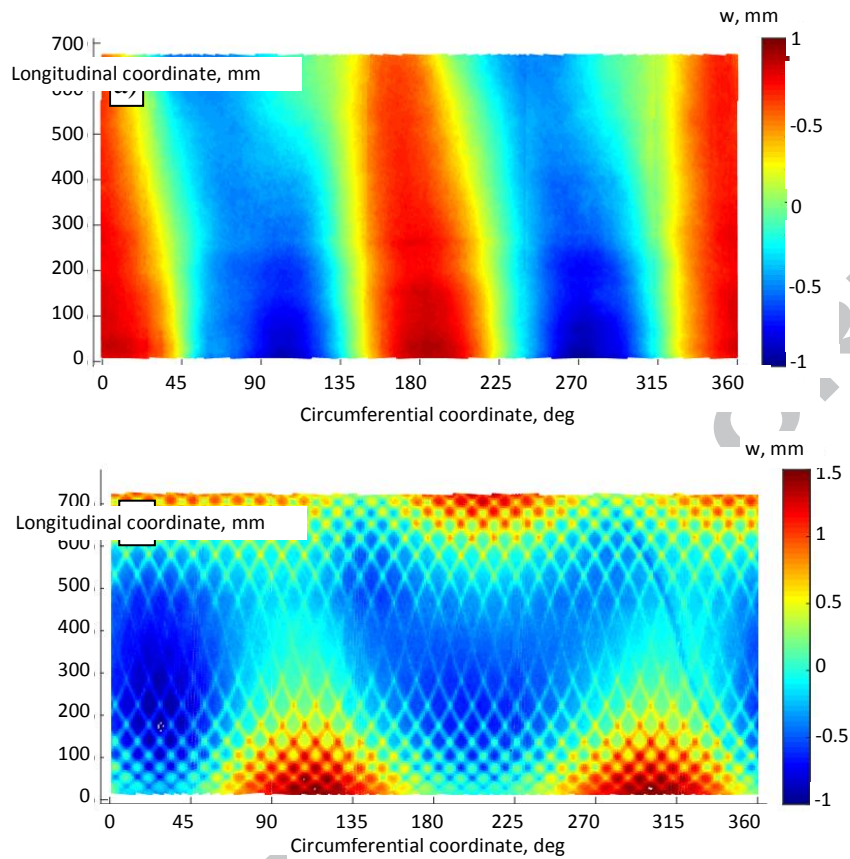
7

Figure 4. Geometrical imperfections plots from DIC system: a) the constant-stiffness cylinder;

b) the variable-stiffness cylinder

Additionally, geometrical imperfections have been measured from inside of the cylinder applying an in-house built rig with laser distance sensor that is shown in Figure 5. The rig for measuring the inner imperfections consists of the console with attached laser distance sensor which rotates around the central shaft by means of the stepper motor and measures the distance at the given angular and height step. Internal measurements are especially important for the variable-stiffness cylinder because changing thickness of the laminate might influence the global imperfection shape.
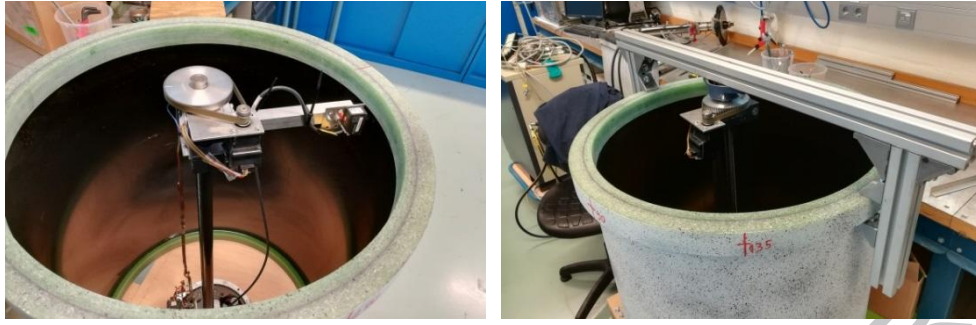
Figure 5. Test set-up for measuring internal geometric imperfections using laser sensor

The outputs of the laser scanner imperfection measurement are plotted in Figure 6. The angle step of the data points are $5^0$ and the height step is 10 mm. The global shape of the imperfection plot matches well with the DIC measurements from Figure 4. The constant-stiffness cylinder is uniformly ovalized along the whole vertical axis, and the variable-stiffness cylinder has several out-of-plane areas at the bottom part.
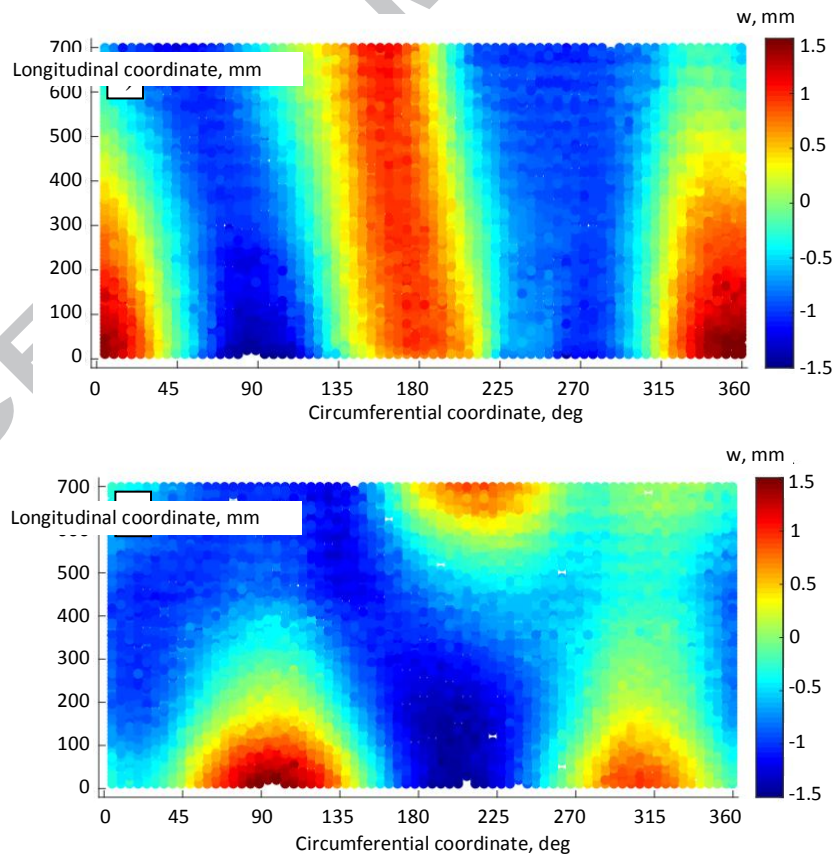


Figure 6. Geometrical imperfections plots obtained by laser sensor:

a) the constant-stiffness cylinder; b) the variable-stiffness cylinder

9

## 4. Numerical models

Numerical analysis of the cylinders was performed in ABAQUS 2017 commercial software. The geometry of the cylinder was based on reduced integration S4R shell-type elements while C3D8R solid elements were used for the end-potting. The material properties of AS4/8552 carbon prepreg material (stated in Table 1) were assigned to the cylinder plies. Isotropic material properties of the end potting were obtained from the epoxy data-sheet [33] where the modulus of elasticity is equal to 4.5 GPa and density equal to 1150 kg/m$^3$.

A mesh size of 10 mm was chosen after performing a mesh sensitivity study. The mesh and boundary conditions of the cylinder are shown in Figure 7. The boundary conditions were set to rigidly link the nodes on the edges of the cylinder to the central reference nodes. Only vertical movement of the upper nodes was allowed. Numerical load/displacement curves were acquired applying displacement constraint on the top reference point and recording reaction force from the bottom reference point. The initial geometrical imperfections obtained by DIC system were integrated in the numerical models. The imperfection shapes magnified by a factor of 50 are shown in Figure 7.c-d. Dynamic implicit analysis was conducted for the compression case and frequency analysis with Lanczos eigensolver was performed for modal analysis.
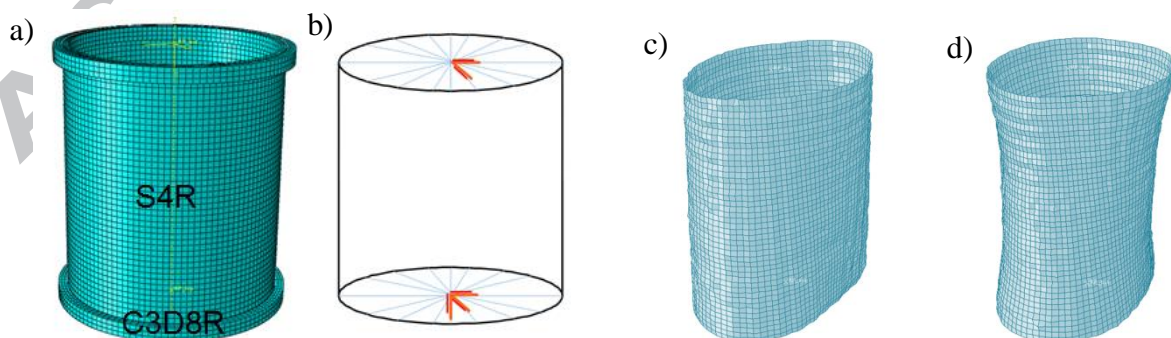


Figure 7. Numerical model: a) mesh; b) boundary conditions; c) magnified (x50) imperfections of the constant-stiffness cylinder; d) magnified (x50) imperfections of the variable-stiffness cylinder

Stiffness variation of the laminate was accounted by a simplified approach of dividing the cylinder area in separate sections along the height, and assigning constant layup and ply number for each section as shown in Figure 8. The fibre angle of the cylinder section was assigned as the average value between the angle at the upper and the lower edge of the section. Additional steered plies were added for the end sections to compensate the effect of overlaps. For example, model 3 has eight additional layers near the ends in section L1 and four additional layers in the following section L2. The models with different number of sections were investigated starting from a coarse model with 2 distinct sections to a finer model with 5 sections.



L1 [±45/±43/±43]s

L2 [±45/±23]s

L1 [±45/±57/±57/±57]s

L2 [±45/±50/±50]s

L3 [±45/±39]s

L4 [±45/±24]s

L1 [±45/±57/±57/±57]s

L2 [±45/±50/±50]s

L3 [±45/±39]s

L4 [±45/±24]s

L5 [±45/±18]s
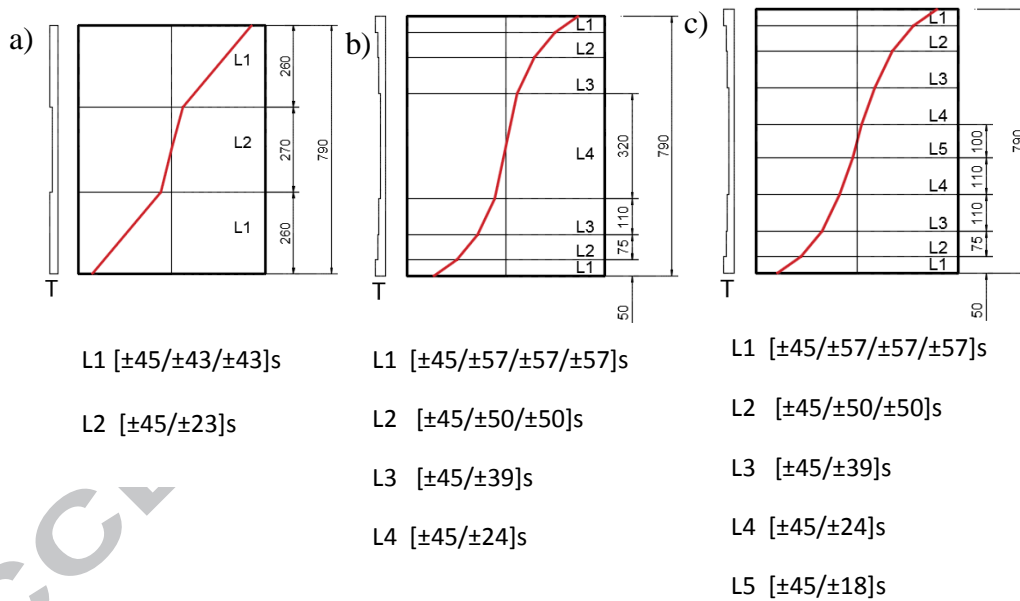
Figure 8. Approximated models of the variable-stiffness cylinder:

a) two sections; b) four sections; c) five sections

## 5. Test set-ups

*Buckling test set-up*

The compression tests were performed using a MTS 3500 servo-hydraulic test machine at Delft University of Technology. The test set-up is shown in Figure 9. Cylinder

specimens were placed on a steel base plate and loaded by hydraulic actuator moving the upper plate by constant velocity equal to 0.25 mm/min. The uniform loading conditions were reached by a self-levelling loading head which was adjusted at low load level. Displacements were measured by two LVDT displacement sensors on both sides of the shell. Analog signals from LVDTs were synchronized with load and time readings in the controlling computer.

Out-of-plane displacement were recorded at the frequency of 1 Hz with two VIC 3D DIC systems, covering front and rear side of the cylinder. Each DIC captured approximately $150^0$ of the cylinder surface.

The tests were performed until buckling of the cylinders. Immediately after buckling the test were manually terminated. The loading plate was slowly returned to the initial position. The sequence of the DIC images were post-processed later to get out-of-plane displacement values using initial positions as reference.
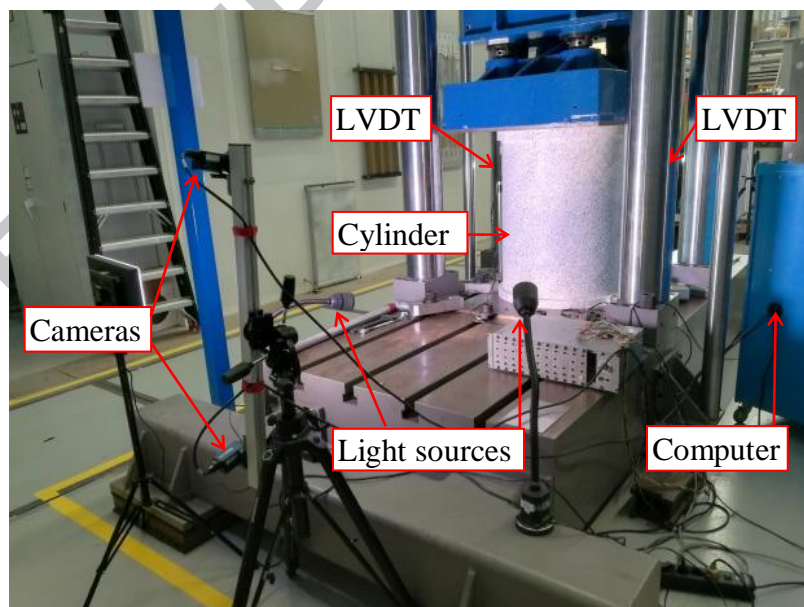


Figure 9. Set-up of the buckling tests with DIC system from the rear side

*Vibration test set-up*

The non-destructive vibration tests were performed using POLYTEC PSV 500 XTRA

scanning laser vibrometer. The main motivation of this activity was to acquire natural frequencies and vibration mode shapes in free-free boundary conditions and to compare them with numerically acquired values. The test set-up and the measuring equipment is shown in Figure 10. It consists of the laser scanning head, data collection unit and the control unit. The excitation of the cylinders in given frequency spectrum from 0 to 800 Hz was performed by using a loudspeaker. The loudspeaker was placed in the lower part of the cylinder, approximately at 1/4 of the axial length. Based on previous experience, this location is optimal as it provides sufficient excitation amplitude for the whole cylinder and allows to reach better signal for the mode shapes with two rows of half-waves (compared to speaker position in the middle of cylinder height) . The advantage of the loudspeaker for exciting the structure is the broad frequency range and convenient installation. Moreover, there is no physical link between speaker and specimen which could influence the response of the shell. The scanned sector of the cylinder covered approximately $160^0$ and consisted of 450 grid points. The cylinder was hanged on thin wires to simulate free-free boundary conditions. The scan of every grid point was repeated at least three times.
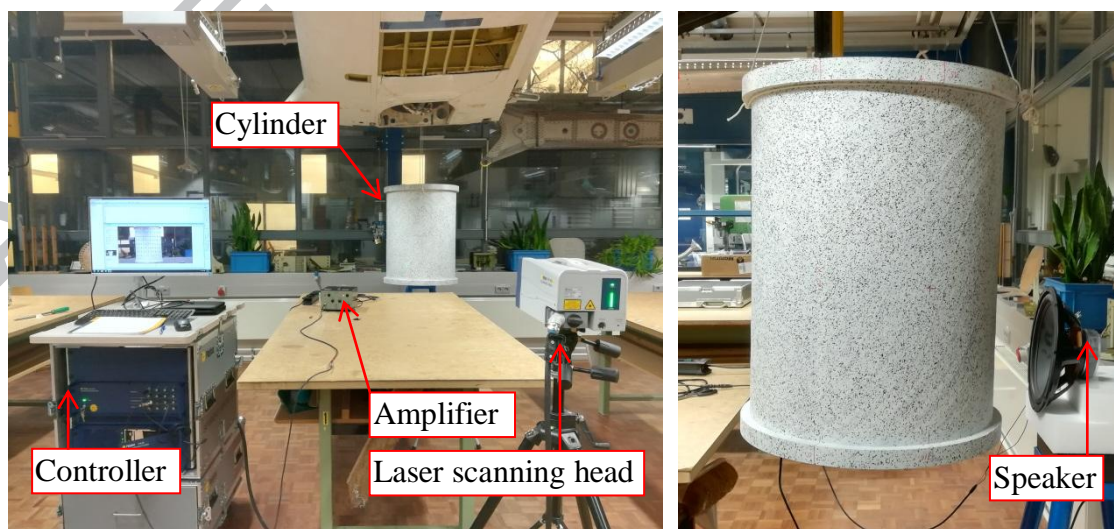


Figure 10. Set-up of POLYTEC PSV 500 equipment for vibration tests

## 6. Results and discussion

The main results of the buckling and vibration tests are summarized here, discussing load-shortening curves, buckling shapes, high-speed video of buckling, natural frequencies and mode shapes.

*Buckling of the cylinders*

The cylinders were loaded in compression until reaching the buckling load, and then gradually unloaded. The load-shortening response was recorded for both cylinders. After buckling the cylinders showed a load drop and a pattern of two-row buckles. The tests also demonstrated good repeatability leading to the same buckling load and buckling shape after several repeated loadings and unloading cycles.

The median load – shortening curve of the constant stiffness cylinder is reported in Figure 11. The experimentally obtained buckling load of the constant-stiffness cylinder is equal to 303 kN at the shortening of 1.65 mm. The range of acquired experimental results performing 10 buckling tests is 301 to 304 kN, with the standard deviation of 1.2 kN. The post-buckling load resistance of this cylinder is equal to 75 kN. The numerical load-shortening curves, obtained by models with the initial geometrical imperfections measured by the DIC system and laser sensor, are marked with dashed lines in the Figure 11. They show a good correlation with the experimental results in terms of stiffness and buckling load. There is a small difference between numerical models with imperfections from DIC system and imperfections from laser scanner. The slightly higher amplitude of the initial geometrical imperfections measured by the laser distance sensor leads to a lower numerical buckling load equal to 318 kN compared to the 339 kN for the numerical model with DIC imperfections. The numerical eigenvalue buckling load of this cylinder is 420 kN. Dividing this value by

experimental buckling load the resulting in knockdown factor is equal to 0.73.

The evolution of the numerical buckling shape is reported in Figure 12. It shows that the global buckling shape evolves from a local buckle in the upper part of the cylinder.
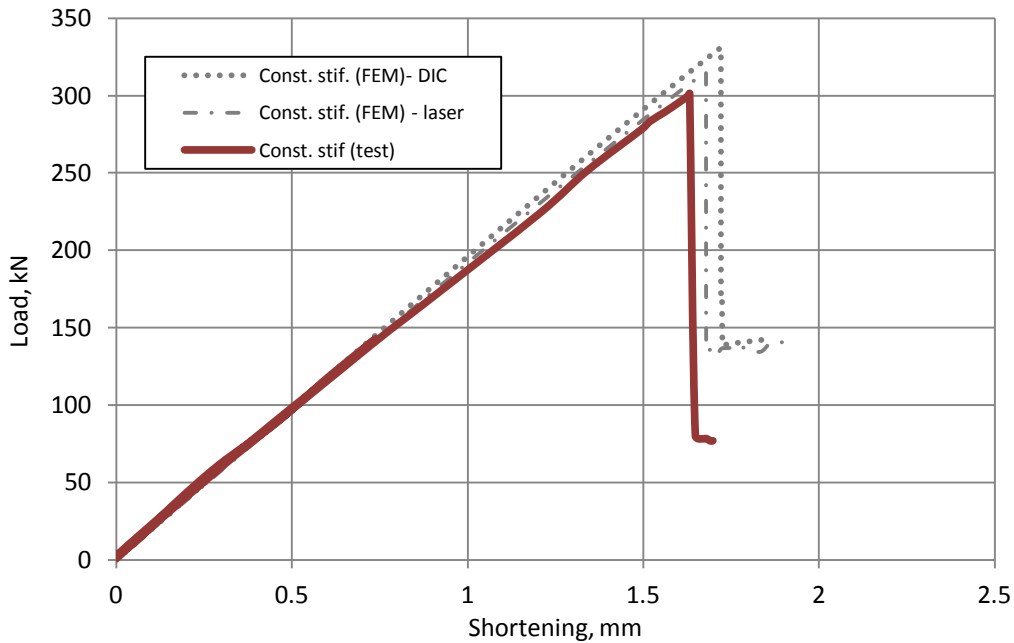


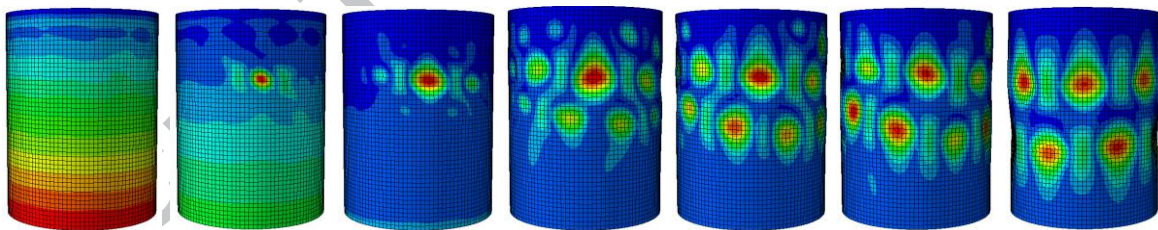Figure 11. Load–shortening curves of the constant-stiffness cylinder



Figure 12. Progression of the buckling shape of the constant-stiffness cylinder

The experimental and numerical load-shortening curves of the variable-stiffness cylinder are shown in Figure 13. The median experimental buckling load for the variable-stiffness cylinder is equal to 208 kN at the shortening of 2.2 mm. The experimental buckling loads after 8 compression tests lie in the range between 206 and 211 kN. The standard deviation of this data set is 1.6 kN. The buckling load and the stiffness of the variable-stiffness cylinder are lower than the constant stiffness cylinder due to not optimized fibre

angles. The post-buckling loads of the variable-stiffness cylinders is equal to 70 kN, which is close to 75 kN load for the constant stiffness cylinder. It is noticeable that post-buckling load of the variable-stiffness cylinders is relatively higher compared to the constant-stiffness cylinder, if divided by the buckling load. Possible explanation of the relatively higher post-buckling load could be the higher bending stiffness of the variable-stiffness cylinder in the post-buckling region.

The three curves of the numerical models represent the different variable-stiffness approximation models. There are only small differences between the numerical model with initial geometrical imperfections from the laser distance sensor and the DIC system, therefore only the results with geometrical imperfections measured by DIC are shown. The model 1, with two sections, has a higher buckling load and stiffness than models 2 and 3 that have 4 and 5 sections, respectively.

In general, the experimental results fit in the range of numerically predicted results. It can be seen that an increase of the number of the sections in the simplified numerical models improve the accuracy of the numerical prediction. Additional sections in the third model provides slight increase in the stiffness, comparing to the curve of the second model.

The numerical eigenvalue buckling load of the variable-stiffness cylinder is closer to the experimental one, compared to the constant-stiffness cylinder. The eigenvalue buckling load of the model 2 is equal to 260 kN, which leads to a shell knockdown factor of 0.81. while for the constant stiffness cylinder it is equal to 0.73. This conclusion aligns well with other literature sources reporting lower sensitivity of variable-stiffness cylinders towards geometrical imperfections [29].
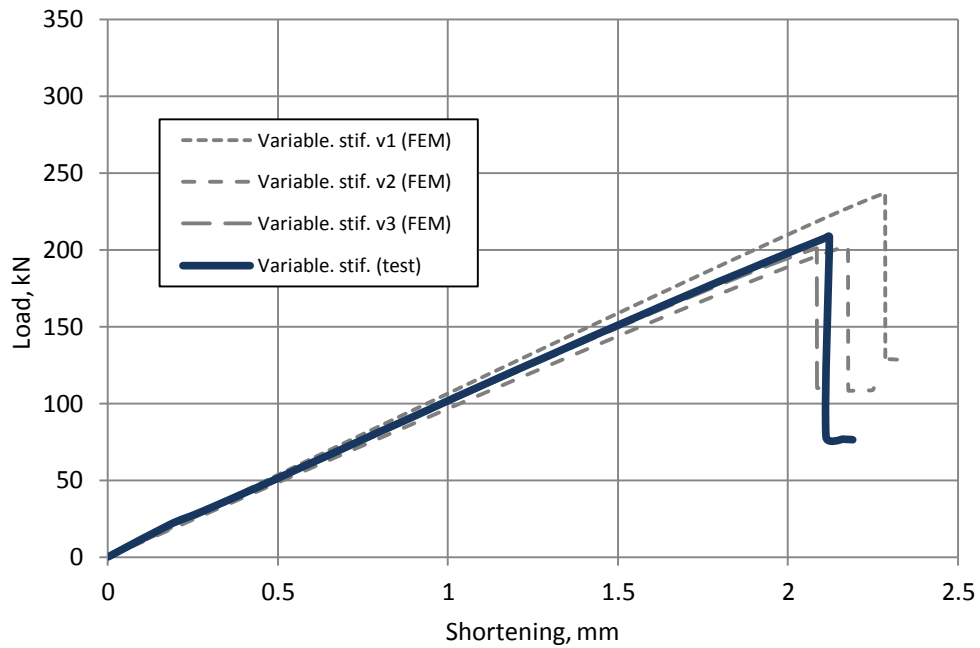
Figure 13. Load–shortening curves of the variable-stiffness cylinders

The step-by-step evaluation of the numerical buckling shape of model 2 with 4 sections is shown in Figure 14. The stable buckling pattern arises from a group of small buckles, which merge into two rows of larger and deeper buckles.
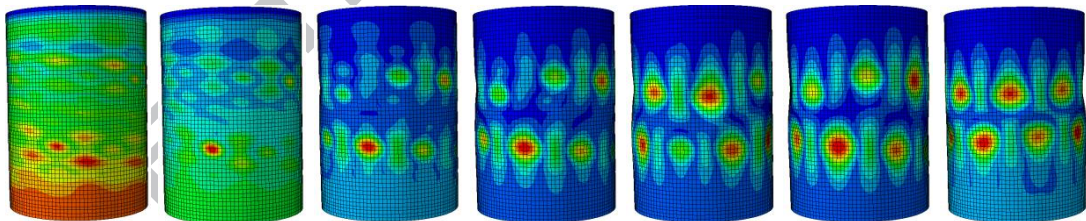


Figure 14. Progression of the buckling shape of the variable-stiffness cylinder

The experimental buckling shapes of the cylinders post-processed by the DIC system are shown in Figure 15. Both cylinders have uniform buckle pattern in two rows, similar colour patterns and also similar amplitudes of the out-of-plane displacements. The maximum experimental outward displacement of the constant-stiffness cylinder is 6.6 mm and inward displacement is -12.2 mm. The variable-stiffness cylinder shows slightly lower displacements of 5.1 mm and -11.5 mm, respectively.

17
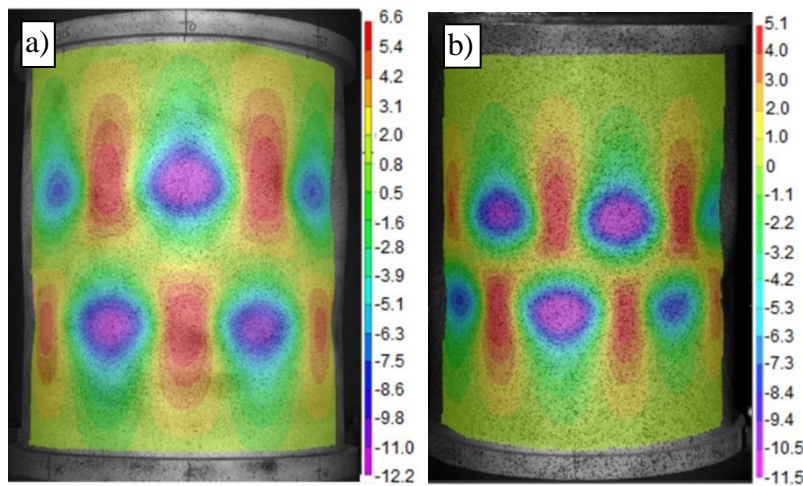
Figure 15. Buckling shapes acquired by DIC system:

a) the constant-stiffness cylinder; b) the variable-stiffness cylinder

The out-of-plane values of the numerical models, shown in Figure 16, have a close match to the experimental results, and the buckling shape and the displacement values are similar. The numerical models have approximately 10% higher maximum inwards and outwards displacement values and a smaller gap between the upper and lower row of buckles.
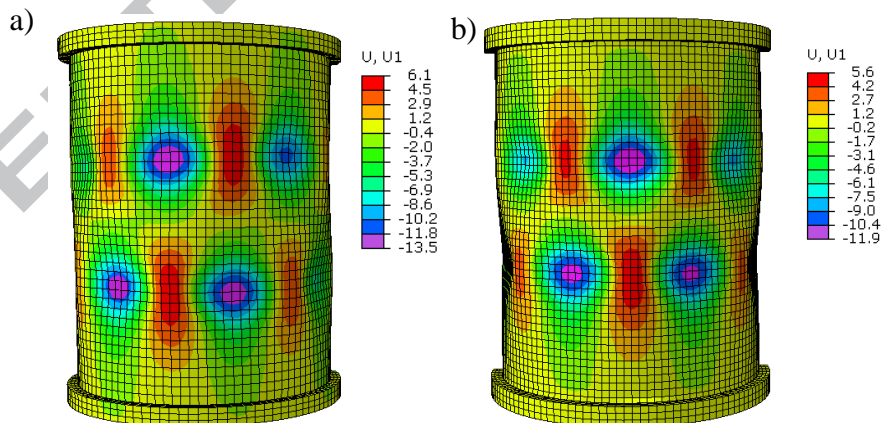


Figure 16. Buckling shapes obtained by the numerical analysis:

a) the constant-stiffness cylinder (load 70 kN, shortening 1.76 mm);

b) the variable-stiffness cylinder (load 75 kN, shortening 2.18 mm)

18

*High speed camera results*

In order to capture the moment of the buckling mode formation, the recording of the compression test was performed by FASTCAM Mini AX200 540K M1 high-speed camera with frame-rate of 20000 frames per second. Given frame rate and lighting conditions allowed to obtain video in resolution of 512x612 pixels. To track the dynamics of the buckling, all the graphic outputs from the high-speed cameras were transferred to Digital Image Correlation (DIC) software VIC 2D. The horizontal displacement of the pixels provides a colour contrast which is close to 3D buckling pattern. Although the intensity of the horizontal displacement is stronger at the sides of the cylinder, than in the middle, it is still possible to track the changes of the buckling pattern.

The sequence of the buckling pattern formation for the constant stiffness cylinder is shown in Figure 17. As it can be seen in the first frame marked as #0, the buckling starts at the lowest left corner of the image. Later the number of small buckles appears over the whole area of the cylinder as shown in the frames #3-14. By progressing further, smaller buckles in the middle part grow but at the ends diminish. In the frames #21-44 it can be seen as several middle sized buckles converge into two rows, which form the final stable shape at #91. Although the final shape is reached in 90 frames, visible oscillation of the surface continues for another 3000 frames that corresponds to 0.15 seconds.

Captured initiation of the buckling mode has certain similarity to the numerical model used to foresee the progression of the buckling mode, as shown in Figure 12. In the numerical model the buckling starts in a single point and later expands across the entire cylinder. In a similar way it can be observed also in the experimental video. Also the oscillation of the final shape has an identical character in the numerical model and the experimental video.
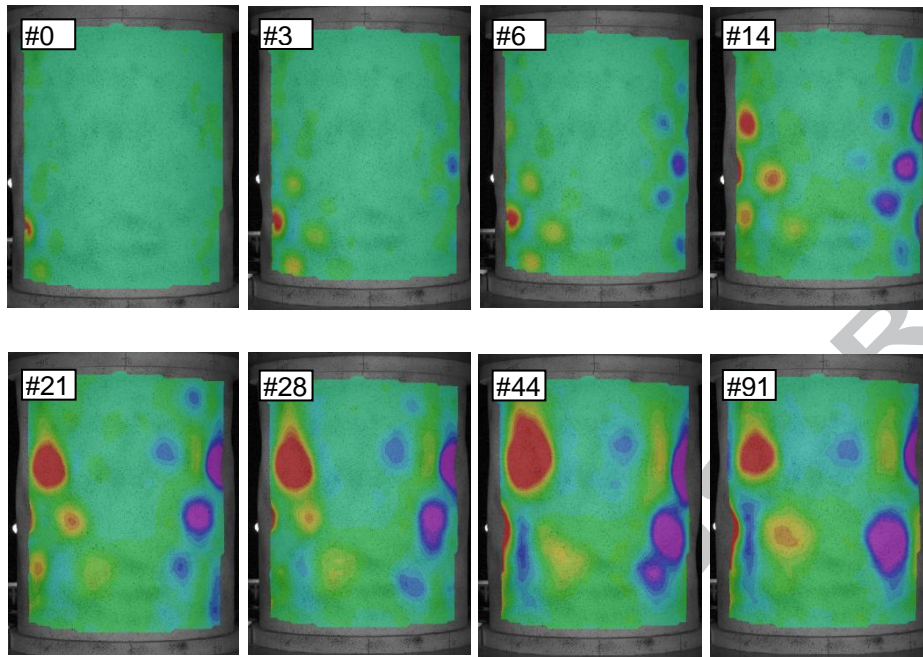
Figure 17. Sequence of the buckling behaviour of the constant-stiffness cylinder,

captured by high-speed camera

High-speed camera video of the variable-stiffness cylinder is shown in Figure 18. Here the buckling starts at the left side of the cylinder in frame #0. Compared to the constant-stiffness cylinder, the small buckles are not spread over the whole surface but mainly concentrated in the middle part. Gradually, the smaller buckles converges into the final pattern in the following frames #6-38. As it can be observed in frames #60-76, two buckles converges into single one. The final symmetrical buckling shape appears only at the frame #190 when clearly visible buckle forms at the lower left corner. The time necessary to form a stable buckling shape for the variable-stiffness cylinder (190 frames) is longer than in the case of the constant-stiffness cylinder (91 frames). It might be caused by lower buckling load of this cylinder.

The gradual development of the buckling shape can be compared to the images from the numerical model reported in Figure 14. In the numerical model as well as in the experimental tests, the buckling starts at the single point and spreads over the whole surface.

20

In the meantime smaller buckles converge into bigger ones and reach the final shape.
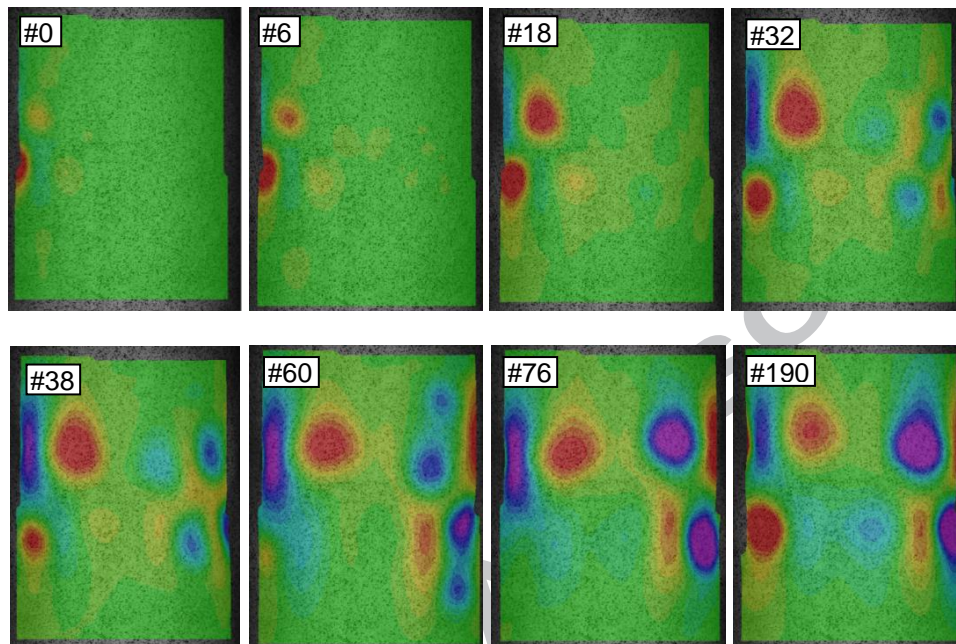


Figure 18. Sequence of the buckling behaviour of the variable-stiffness cylinder,

captured by high-speed camera

*Vibration analysis*

The response magnitude and frequency curves for both cylinders are plotted in Figure 19. The curves in Figure 19 are from the tests with the highest number of grid-points on the surface. Previously, tests with coarser grid were performed and they provided almost identical results. The first and second vibration modes of the two cylinders have overlapping frequencies of 84 and 97 Hz, respectively. The following response peaks for the variable-stiffness cylinder are shifted right from the constant-stiffness cylinder. This can be explained by the lower stiffness of the variable fibre layout.
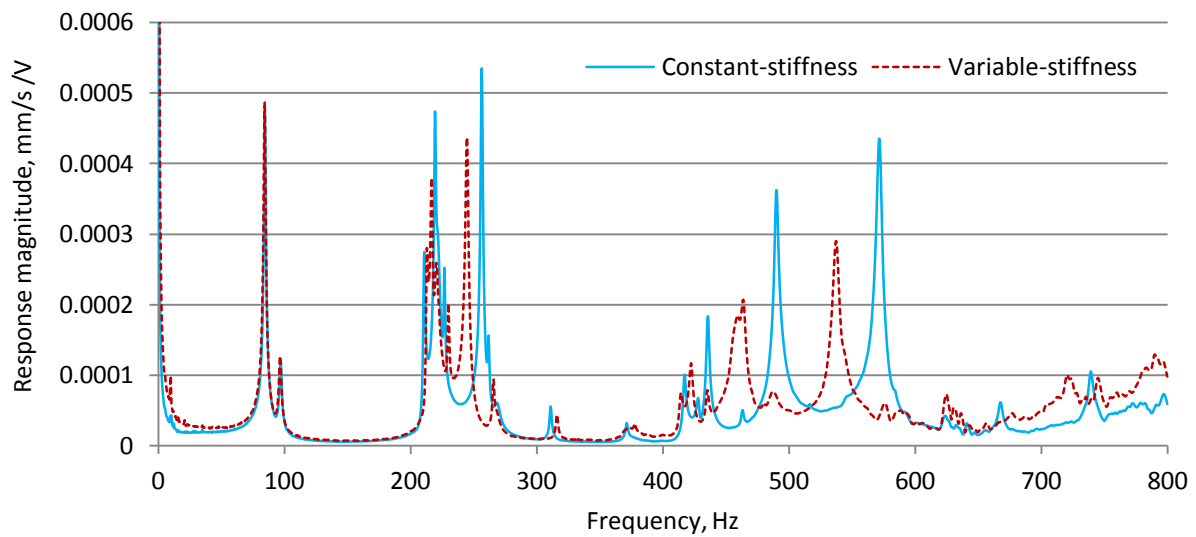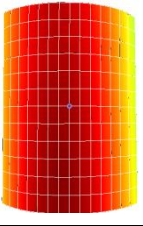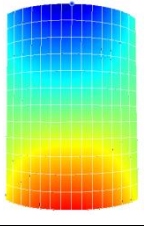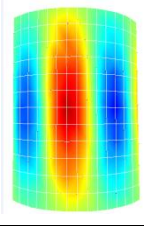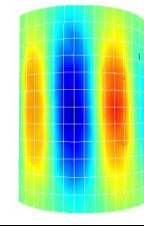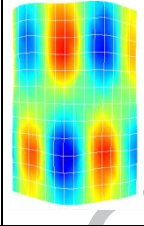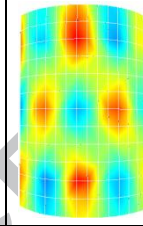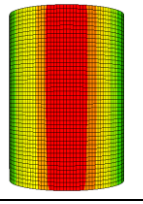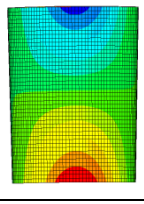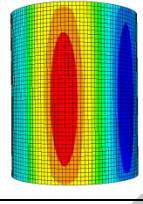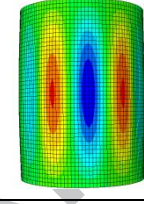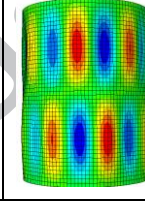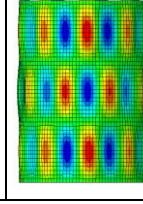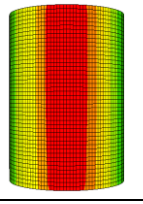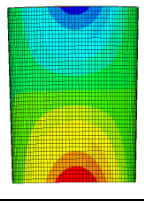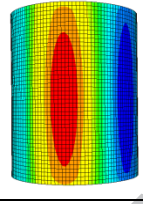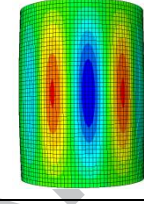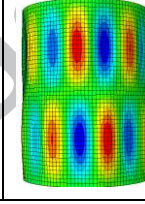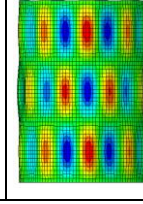
Figure 19. Response magnitude-frequency curves for the constant and variable-stiffness cylinders

The mode shapes acquired during the tests are compared to the numerical ones in Table 2 and Table 3 for the constant and variable-stiffness cylinder, respectively. The blue colour areas represent the outward displacement, while the red areas the inward displacement. Only unique mode shapes, by displacement pattern, are displayed in Table 2 and 3 which means that number of similar shapes exist between them. The obtained results can be used as an additional layer of validation for the approximated model of variable ply layout.
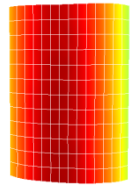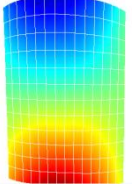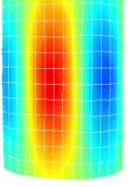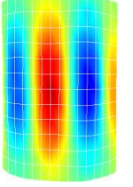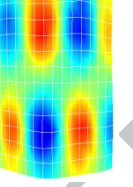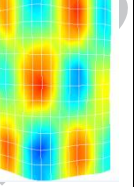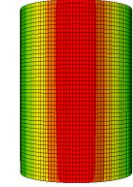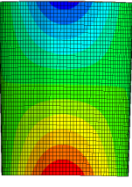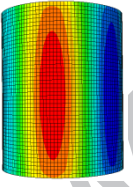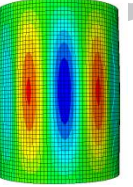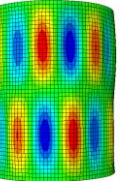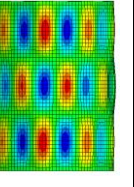
The results of the constant-stiffness cylinder in Table 2 shows that the complexity of the shape increases as the frequency number grows. The mode shape 5 has the closest visual pattern to the buckling shape of the cylinder in compression depicted in Figure 15. At the end of the frequency spectrum (668 Hz) it was possible to capture the mode with three rows of buckles. The numerical results have a close matching frequency and shape, except mode shape 5 with 13% deviation from the experimentally measured natural frequency.

22

Table 2. Mode shapes and natural frequencies of the constant-stiffness cylinders

| Nr | 1 | 2 | 3 | 4 | 5 | 6 |
|---|---|---|---|---|---|---|
| Freq, Hz | 84 | 97 | 211 | 227 | 422 | 668 |
| Exp shape |  | | | | | |
| Freq, Hz | 83 | 94 | 224 | 228 | 458 | 697 |
| FEM shape |  | | | | | |

The results of the variable-stiffness cylinder in Table 3 have mode shapes and frequencies similar to the constant-stiffness cylinder. The numerical model is capable of capturing all the mode shapes although the coarse experimental grid step makes the displacements shapes slightly blurred. The natural frequencies predicted by the numerical model are below the experimentally measured values for the first two mode shapes and are higher for the shapes 3-6. The largest deviation is for the last mode shape – equal to 16% for the numerical model 3 with 5 sections. As it was noticeable in the load-shortening curves in Figure 13, the refinement of the model adding one section does not have significant impact on the free vibration results.

Table 3. Mode shapes and natural frequencies of the variable-stiffness cylinders

| Nr | 1 | 2 | 3 | 4 | 5 | 6 |
|---|---|---|---|---|---|---|
| Freq, Hz | 84 | 96 | 217 | 230 | 423 | 666 |
| Exp shape |  | | | | | |
| Model 1 | 80 | 90 | 210 | 243 | 488 | 787 |
| Model 2 | 82 | 92 | 221 | 248 | 511 | 786 |
| Model 3 | 82 | 92 | 221 | 251 | 509 | 791 |
| FEM shape |  | | | | | |

## 7. Conclusions

In the current study, buckling and free-vibration tests and analysis were performed on two CFRP cylinders: a constant-stiffness and a variable-stiffness cylinder. The compression tests were conducted using a hydraulic test rig with displacement driven control, capturing the buckling behaviour with DIC systems and high-speed camera. The vibration analysis were performed with free-free boundary conditions measuring natural frequencies and mode shapes. Prior to the tests, initial geometric imperfections were measured from outside and inside and later introduced in the numerical model.

Both cylinders shared some common mechanical behaviour traits like elastic load-shortening curves, sudden loss of load bearing capacity at buckling and similar buckling shape. In addition, good repeatability of the buckling load was reached for both cylinders. The variable-stiffness cylinder showed lower sensitivity to initial geometrical imperfections compared to the constant-stiffness cylinder.

24

A simplified numerical model for the variable-stiffness cylinder was developed during the study. Comparison of the experimental and numerical results show that the simple approximation model is capable to predict buckling load and mode shapes for the shells with variable fibre angles.

Considering that experimental data on variable-stiffness cylinders are scarce, the research provides useful information for further model validation and implementation of the variable-stiffness laminates in aerospace structures.

Future work will be directed to develop accurate numerical modelling for fibre steered shells, that is essentially for the further optimisation of the variable-stiffness composites.

## References

1. Evans DO. Fiber placement. Handbook of Composites. Springer; 1998.

2. Morey B. Automating composites fabrication. Manufacturing Engineering 2008;140(4).

3. Hyer MW, Lee H. The use of curvilinear-fiber format to improve buckling resistance of composite plates with central holes. Composite Structures 1991; 18(3): 239–261.

4. Hyer MW, Charette RF. Use of curvilinear fiber format in composite structure design. AIAA Journal 1991;29(6):1011-1015.

5. Schueler K, Hale R. Object-oriented implementation of an integrated design and analysis tool for fiber-placed structures. Proceedings of the 43rd AIAA/ASME/ASCE/AHS/ASC Structures, Structural Dynamics and Materials Conference, Denver, CO, 22-25 April 2002. Paper number: 1223.

6. Tatting  BF, Gurdal Z. Automated finite element analysis of elastically-tailored plates. NASA/CR-2003-212679, December 2003.

7. van Campen J, Kassapoglou C, Gurdal Z. Generating realistic laminate fiber angle

25

distributions for optimal variable-stiffness laminates. Composites Part B: Engineering 2012;43(2): 354–360.

8. Peeters D, Abdalla M. Design guidelines in nonconventional composite laminate optimization. Journal of Aircraft 2017;54(4):1454-1464.

9. Marouene A, Boukhili R, Chen J, Yousefpour A. Buckling behavior of variable-stiffness composite laminates manufactured by the tow-drop method. Composite Structures 2016;139:243-253.

10. White SC, Raju PM, Weaver PM. Initial post-buckling of variable-stiffness curved panels. Journal of the Mechanics and Physics of Solids 2014;71(1) 132-155.

11. Castro SGP, Donadon MV, Guimarães TAM. ES-PIM applied to buckling of variable angle tow laminates. Composite Structures 2019;209:67-78.

12. Ghiasi H, Fayazbakhsh K, Pasini D, Lessard L. Optimum stacking sequence design of composite materials. Part II: Variable-stiffness design. Composite Structures 2010;93(1):1-13.

13. Sabido A, Bahamonde L, Harik R, van Tooren MJL. Maturity assessment of the laminate variable-stiffness design process. Composite Structures 2017;160:804-812.

14. Lozano GG, Tiwari A, Turner C, Astwood S. A review on design for manufacture of variable-stiffness composite laminates. Proceedings of the Institution of Mechanical Engineers, Part B: Journal of Engineering Manufacture 2016;230(6):981-992.

15. Bisagni C. Numerical analysis and experimental correlation of composite shell buckling and post-buckling. Composites Part B 2000;31(8):655-667.

16. Bisagni C, Cordisco P. An experimental investigation into the buckling and post-buckling of CFRP shells under combined axial and torsion loading. Composite Structures 2003;60(4):391-402.

17. Bisagni C, Vescovini R. Fast tool for buckling analysis and optimization of stiffened panels. Journal of Aircraft 2009;46(6):2041-2053.

18. Eglitis E, Kalnins K, Ozolinsh O. The influence of loading eccentricity on the buckling of axially compressed imperfect composite cylinders. Mechanics of Composite Materials 2010;46(5):483-492.

19. Kalnins K, Arbelo MA, Ozolins O, Skukis E, Castro SGP, Degenhardt R. Experimental nondestructive test for estimation of buckling load on unstiffened cylindrical shells using vibration correlation technique. Shock and Vibration 2015; Paper number 729684.

20. Wu KC, Stanford BK, Hrinda GA, Wang Z, Martin RA, Kim HA. Structural assessment of advanced composite tow-steered shells. Proceedings of the 54th AIAA/ASME/ASCE/AHS/ASC Structures, Structural Dynamics and Materials Conference, Boston, Massachussetts, 2013; 1-20. Paper number: 1769.

21. Wu KC, Turpin JD, Stanford BK, Martin RA. Structural performance of advanced composite tow-steered shells with cutouts. Proceedings of the 55th AIAA/ASMe/ASCE/AHS/SC Structures, Structural Dynamics, and Materials Conference, National Harbor, Maryland, 2014. Paper number: 1056.

22. White SC, Weaver PM, Wu KC. Post-buckling analyses of variable-stiffness composite cylinders in axial compression. Composite Structures 2015; 123(1): 190-203.

23. Blom AW, Stickler PB, Gürdal Z. Optimization of a composite cylinder under bending by tailoring stiffness properties in circumferential direction. Composites Part B: Engineering 2010;41(2):157-165.

24. Rouhi M, Ghayoor H, Fortin-Simpson J, Zacchia TT, Hoa SV, Hojjati M. Design, manufacturing, and testing of a variable-stiffness composite cylinder. Composite Structures 2018;184:146-152.

27

25.  Rouhi M, Ghayoor H, Hoa SV, Hojjati M. Effect of structural parameters on design of variable-stiffness composite cylinders made by fiber steering. Composite Structures 2014;118(1):472-481.

26. Khani A, Abdalla MM, Gürdal Z. Circumferential stiffness tailoring of general cross section cylinders for maximum buckling load with strength constraints. Composite Structures 2012; 94(9):2851-2860.

27. Güldü S, Kayran A. Maximizing buckling load factors of fiber-placed composite cylindrical shells by particle swarm optimization. Proceedings of the 56th AIAA/ASCE/AHS/ASC Structures, Structural Dynamics and Materials Conference, Kissimmee, Florida. 2015. Paper number: 0449.

28. Sun M, Hyer MW. Use of material tailoring to improve buckling capacity of elliptical composite cylinders, AIAA Journal 2008; 46(1):770-782.

29. White SC, Weaver PM. Towards imperfection insensitive buckling response of shell structures-shells with plate-like post-buckled responses, Aeronautical Journal 2016; 120: 233-253.

30. VIC-3D v7 Reference Manual, Correlated Solutions, 2016.

31. ABAQUS/Standard User's Manual. Version 2017 ABAQUS. Inc. USA, 2017.

32. HexPly prepreg Technology, Hexcel Corporation, 2013.

33. https://www.swiss-composite.ch/pdf/t-Epoxydharz-L20-e.pdf Technical data sheet of L-20 epoxy. Accessed 10.11.2018